MATERIALS SCIENCE

Atomic-resolution structural and spectroscopic evidence for the synthetic realization of two-dimensional copper boride

Hui Li[1], Qiyuan Ruan[2], Cataldo Lamarca[1], Albert Tsui[1], Boris I. Yakobson[2]*, Mark C. Hersam[1,3,4]*

Since the first realization of borophene on Ag(111), two-dimensional (2D) boron nanomaterials have attracted substantial interest because of their polymorphic diversity and potential for hosting solid-state quantum phenomena. Here, we use atomic-resolution scanning tunneling microscopy (STM) and field-emission resonance (FER) spectroscopy to elucidate the structure and properties of atomically thin boron phases grown on Cu(111). Specifically, FER spectroscopy reveals charge transfer and electronic states that strongly differ from the decoupled borophene phases observed on silver, suggesting that the deposition of boron on copper results in strong covalent bonding characteristic of a 2D copper boride. This conclusion is reinforced by detailed STM characterization of line defects that are consistent with density functional theory calculations for atomically thin Cu_8B_{14}. This evidence for 2D copper boride is likely to motivate future synthetic efforts aimed at expanding the relatively unexplored family of atomically thin metal boride materials.

INTRODUCTION

The pioneering realization of borophene polymorphs on silver (*1*, *2*) demonstrated the feasibility of growing boron nanomaterials in two-dimensional (2D) forms, inspiring additional efforts to achieve borophene synthesis on other substrates including Al (*3*), Au (*4*), Ir (*5–7*), Cu (*8–11*), and Ru (*12*). A key element in stabilizing borophene is charge transfer with the substrate (*13*), where metals can act as a charge reservoir to compensate for the fact that elemental boron materials struggle to satisfy the octet rule. While many efforts to diversify the set of growth substrates have resulted in distinct borophene phases, another possibility is that boron will covalently bond with the underlying metal [which is the reason Cu was not favored as a substrate in the first theory (*14*) of borophene synthesis] to form atomically thin metal borides. Distinguishing between borophene and 2D metal borides is often challenging, necessitating the utilization of multiple atomic-resolution structural and spectroscopic characterization methods.

Of particular interest is the product of atomically thin boron deposition on Cu(111), where different interpretations of the observed structure have been reported including single-layer borophene (*7–9*), bilayer borophene (*11*), and 2D copper boride (*15–18*). Beyond the well-known superconductor MgB_2 (*19*, *20*), crystalline metal borides with layered structures are rare, which implies that 2D metal borides (MBenes) are relatively unexplored compared to other 2D materials, despite theoretical predictions that they should have superlative electronic, magnetic, and mechanical properties (*21*, *22*). Therefore, it is of high interest to show strong evidence for the synthetic realization of 2D copper boride to motivate future efforts aimed at expanding the relatively unexplored family of atomically thin metal boride materials.

Here, we use atomic-resolution scanning tunneling microscopy (STM) and field-emission resonance (FER) spectroscopy to characterize the structure and properties of 2D boron phases grown on Cu(111). FER spectroscopy reveals charge transfer and electronic states that are consistent with strong covalent bonding between boron and copper that is characteristic of a 2D copper boride. Moreover, STM characterization of line defects agrees with density functional theory (DFT) calculations for atomically thin Cu_8B_{14} as opposed to a distinct borophene adlayer. In this manner, this work not only clarifies the structure of atomically thin boron deposited on Cu(111) but also provides a methodology for differentiating borophene from atomically thin borides on other metal substrates.

RESULTS

FER spectroscopy of atomically thin boron on Cu(111)

Atomically thin boron phases on Cu(111) single crystals are achieved by electron-beam deposition from a high-purity boron rod onto an atomically clean Cu(111) surface maintained at a substrate temperature of ~550°C in ultrahigh vacuum (UHV). Figure 1A shows a representative STM image of the Cu(111) surface after atomically thin boron deposition, in which a spatial derivative along the horizontal direction is taken to enhance imaging contrast. A highly ordered 2D sheet is observed with a morphology consistent with earlier reports as mentioned above. The height profile extracted from a zoomed-in area (fig. S1) compares the thickness of the 2D sheet with a pristine copper step height, confirming submonolayer coverage. With a sharper tip, an atomic-resolution STM image is obtained. As seen in Fig. 1B, the topography has a zigzag superstructure with ~90° turns. The higher local density of states (LDOS) due to the compressed atomic spacing at the turning points and additional longer-range order induced by the underneath copper layer lead to the observed brightness variations at these corners. Because of convolution between electronic and physical structures, the STM image alone is insufficient to identify the identity of this zigzag phase. Consequently, we will refer to the as-grown structure as B/Cu.

[1]Department of Materials Science and Engineering, Northwestern University, Evanston, IL 60208, USA. [2]Department of Materials Science and NanoEngineering, Rice University, Houston, TX 77005, USA. [3]Department of Chemistry, Northwestern University, Evanston, IL 60208, USA. [4]Department of Electrical and Computer Engineering, Northwestern University, Evanston, IL 60208, USA.
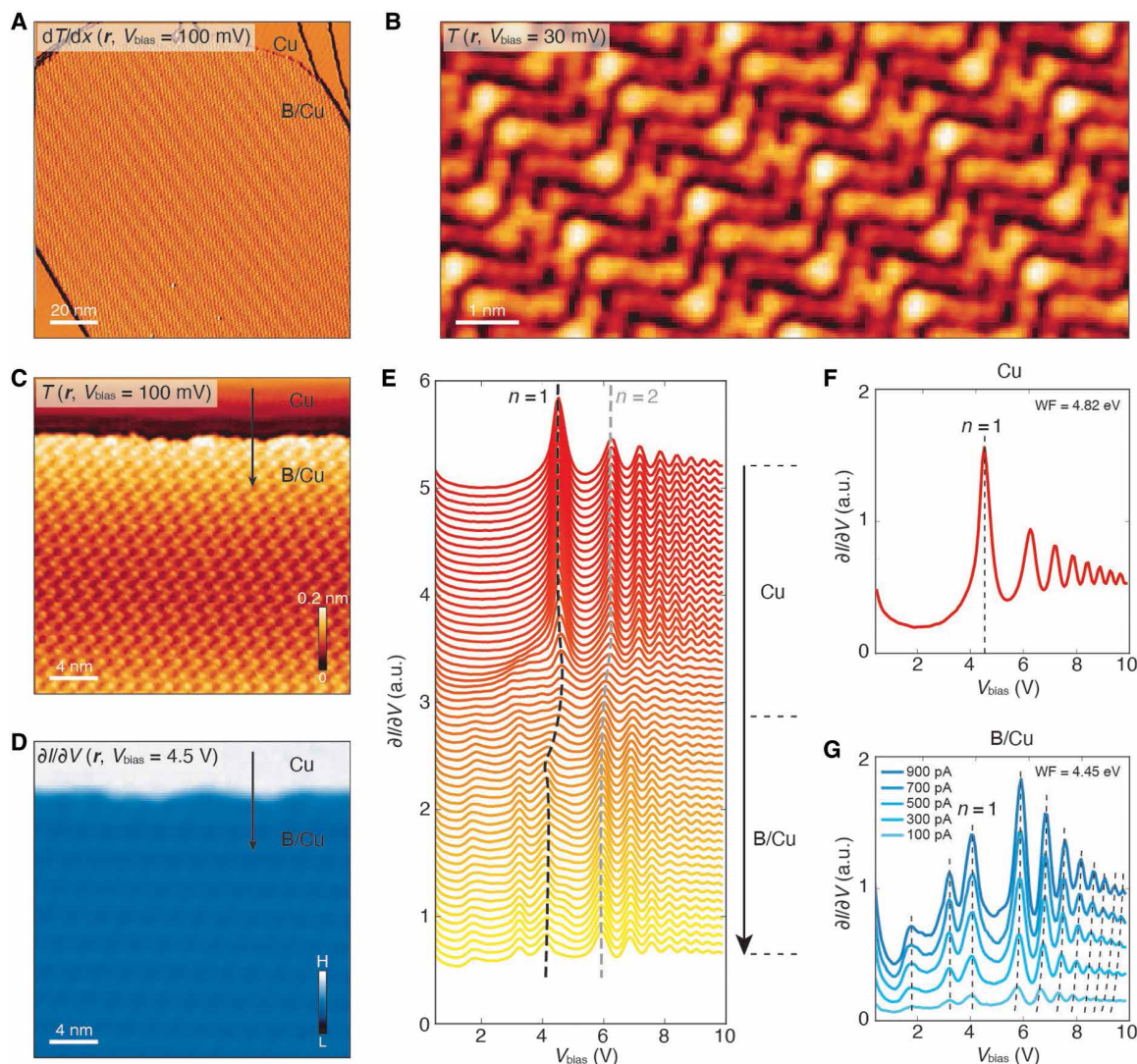*Corresponding author. Email: biy@rice.edu (B.I.Y.); m-hersam@northwestern.edu (M.C.H.)

Fig. 1. Boron deposition on Cu(111) surface and FER measurements. (**A**) Derivative STM topography (V_{bias} = 100 mV and $I_{setpoint}$ = 100 pA) of the as-grown B/Cu struc-ture on a Cu(111) substrate. (**B**) Atomic-resolution STM image (V_{bias} = 30 mV and $I_{setpoint}$ = 100 pA) of the B/Cu structure. (**C**) STM topography (V_{bias} = 100 mV and $I_{setpoint}$ = 300 pA) of a domain boundary between B/Cu and pristine Cu(111). (**D**) Constant-current $\partial I / \partial V$ map at V_{bias} = 4.5 V extracted from FER spectroscopic mapping taken in the same area as (C). (**E**) A series of FER spectra across the boundary [black arrows in (C) and (D)]. The black and gray dashed lines trace the evolution of the n = 1 and n = 2 FER peaks, respectively. a.u., arbitrary units. (**F**) The averaged FER spectrum on a 1 nm–by–1 nm area of Cu(111). The measured work function (WF) is 4.82 eV. (**G**) FER spectra of B/Cu at different tip-sample distances, where the bias voltage is fixed at 100 mV and the setpoint currents vary from 100 to 900 pA. Each spectrum is averaged over the same 1 nm–by–1 nm square on a B/Cu region. The measured WF is 4.45 eV.

Since a well-defined boundary exists between pristine Cu(111) and the B/Cu domain, characterization of the electronic properties with spatially resolved spectroscopic measurements in this area is desirable, as it can ensure that information is extracted under the same tip condition. In particular, we use FER spectroscopy to ex-tract spatially resolved electronic properties. FER spectroscopy is realized using the constant-current mode of scanning tunneling spectroscopy (STS), where both $\partial I / \partial V$ and $\partial z / \partial V$ signals provide a series of clear resonance peaks. Since its early demonstrations (*23*, *24*), FER spectroscopy has proven to be a highly reliable and insightful method for the study of local work function (LWF) varia-tions of engineered metal surfaces (*25–29*). In our case, we per-formed FER spectroscopic mapping (see movie S1 for the full video)

over the field of view in Fig. 1C where a $\partial I / \partial V$ spectrum up to 10.0 V is registered on each point of a grid map using a lock-in amplifier. A slice of the map taken at 4.5 V is shown in Fig. 1D that highlights the FER intensity difference between the Cu(111) and B/Cu regions. These systematic distinctions can be further observed from a series of spectra (Fig. 1E) extracted along the black arrow in Fig. 1 (C and D), where the black and gray lines trace the evolution of the first- and second-order Rydberg peaks, respectively. The peaks that cor-respond to the image potential states exhibit an unambiguous shift to lower energies from the pure Cu(111) area to the B/Cu area. Since image potential states are positively correlated with the LWF (*30*), the FER spectra enable a direct visualization of LWF shifts. A quan-titative extraction of the LWF can be achieved by fitting to the

following equation based on resonant tunneling in the Fowler-Nordheim regime (*31*)

$$eV_n = \phi + \left(\frac{3\pi\hbar eF}{2\sqrt{2m}}\right)^{2/3} n^{2/3} \qquad (1)$$

where V_n is the energy of the peak of order n and the effective electric field (F) is approximated as a constant. The LWF (ϕ) is then extracted by fitting the $n > 2$ peaks with respect to $n^{2/3}$. This fitting results in locally averaged work functions of $\phi_{Cu} \sim 4.82$ V and $\phi_{B/Cu} \sim 4.45$ V. The Cu(111) LWF is in agreement with previous literature (*32*), thus validating the tip condition. The smaller LWF of B/Cu compared to Cu(111) is consistent with the peak position shifts in Fig. 1E. It is, however, contrary to the cases of most distinct borophene phases on metal surfaces, in which the charge transfer from the metal substrate to the borophene layer results in a surface dipole with an increased LWF (*29*, *33*). Therefore, the FER measurements and LWF results suggest that the observed adlayer is not likely to be borophene but rather a surface metal boride.

Another notable feature in the FER spectra is the presence of additional peaks below 4.0 V that only exist in the B/Cu region. In the FER spectrum of the pristine Cu(111) region (Fig. 1F), the $n = 1$ peak is found at ~4.5 V with no additional features other than resonance peaks, which is consistent with previous studies on the Cu(111) surface (*24*, *26*). To reveal the nature of the low-energy peaks in the B/Cu FER spectra, we performed a measurement as a function of tip-sample distance by varying the tunneling junction

resistance at a fixed point. As shown in Fig. 1G, the higher-order FER peaks shift when the setpoint current changes (setpoint bias voltage held fixed at 100 mV), which is expected for resonance states (*29*). On the other hand, the peak positions near 1.96 and 3.35 V are almost constant, suggesting that these electronic states are providing additional information about the B/Cu region beyond LWF. In principle, constant-height dI/dV measurements should also be able to resolve these electronic states as demonstrated in fig. S2. However, the overall high LDOS makes it difficult to precisely extract the constant-height dI/dV peaks. Therefore, FER spectroscopy is the superior approach in this context. The nearly invariant low-energy FER spectral features for B/Cu are similar to copper nitride films with varied stoichiometries (*34*–*36*). In addition, constant-current $\partial I/\partial V$ measurements at negative energies for B/Cu (fig. S3) exhibit similar peaks compared to Cu_3N (*36*). These spectral similarities between B/Cu and covalently bonded copper nitrides suggest that the B/Cu region is likely a covalently bonded copper boride.

DFT calculations and simulations
To investigate the B/Cu system from a theoretical perspective, we performed DFT calculations and simulations on multiple plausible B/Cu structures including a distinct single-layer borophene phase and a covalently bonded Cu_8B_{14} copper boride phase. In particular, $v_{1/6}$ borophene (β_{12}) and Cu_8B_{14} copper boride on Cu(111) are shown in Fig. 2 (A and B), respectively. The $v_{1/6}$ borophene layer has a rectangular unit cell, whereas the Cu_8B_{14} consists of a superlattice ($a \sim 2.18$ nm and $b \sim 1.60$ nm) depicted by a red rhomboid in Fig.
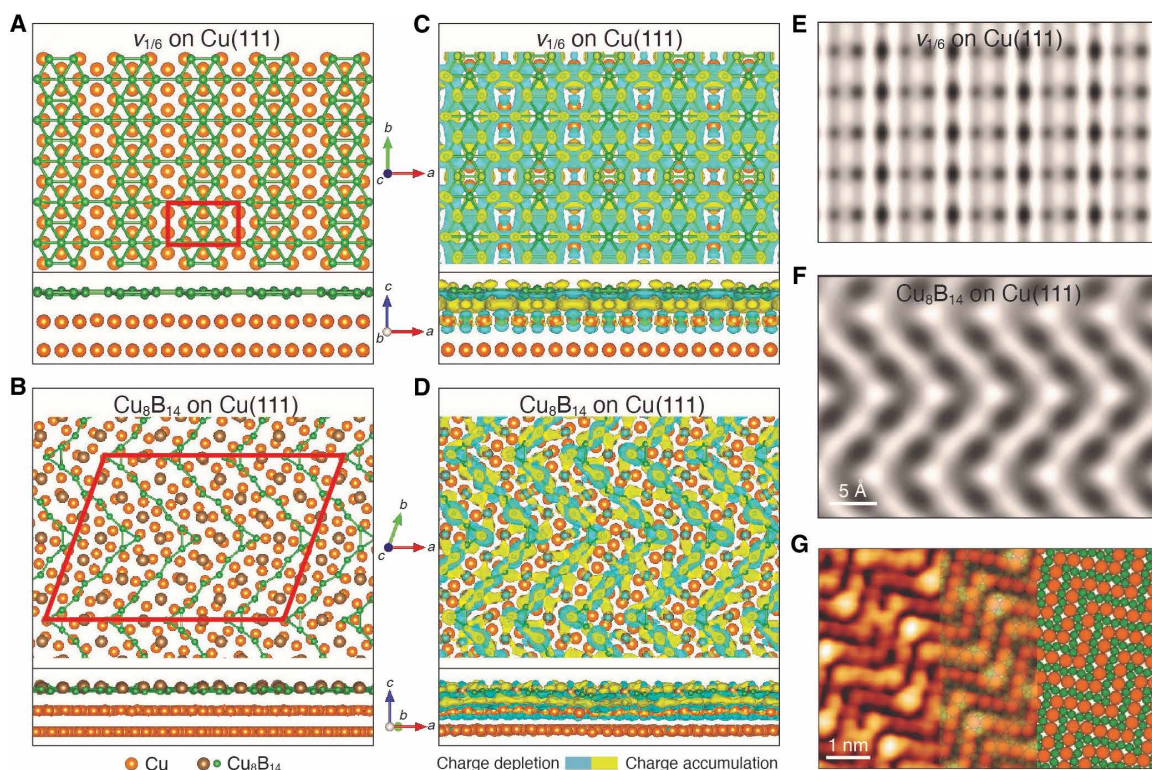

Fig. 2. DFT calculations of borophene and copper boride on Cu(111). (**A**) Top and side view of $v_{1/6}$ borophene on top of Cu(111). The red rectangle depicts the unit cell of $v_{1/6}$ borophene. (**B**) Top and side view of Cu_8B_{14} copper boride on top of Cu(111). The red rhomboid depicts a superlattice in which the corner B atoms sit atop the second-layer Cu atoms. (**C** and **D**) Calculated charge redistribution of the corresponding structures in (A) and (B), respectively. (**E** and **F**) Simulated STM images of $v_{1/6}$ borophene and Cu_8B_{14} copper boride, respectively. (**G**) Experimental STM topography (cropped from Fig. 1B) overlapped with the Cu_8B_{14} structural model.

2B, in which the corner boron atoms sit atop the second-layer copper atoms. From the side view of Cu_8B_{14}, it can be seen that the B atoms are imbedded in the first-layer Cu atoms and inhomogeneous strain exists because of the lattice mismatch. Figure 2 (C and D) depict the DFT-calculated charge redistributions in these two scenarios. Clear differences in charge transfer are apparent between $v_{1/6}$ borophene and Cu_8B_{14}, with the Cu_8B_{14} case resulting in a decreased LWF that is consistent with the aforementioned experimental observation. Simulated STM images of $v_{1/6}$ borophene and Cu_8B_{14} are also provided in Fig. 2 (E and F), respectively. The simulated STM image of Cu_8B_{14} shows a periodic zigzag pattern that closely matches the experimental STM image. Figure 2G further highlights the agreement between experiment and theory for Cu_8B_{14} by overlapping the atomically resolved experimental STM image (reproduced from Fig. 1B) with the DFT-calculated Cu_8B_{14} structure. We note that previous literature (16–18) has also suggested the Cu_8B_{14} structure, although the ambiguity resulting from the convolution of physical and electronic structure in STM imaging has led to a lack of consensus on this structure, thus necessitating further evidence to firmly establish the structure of B/Cu.

Line defects for atomically thin boron on Cu(111)

Previous reports for atomically thin boron deposition on copper have focused on the pristine regions of the 2D layers without explicitly addressing defect structures, despite the value of defect structures in identifying the atomic structure of surface adlayers (37, 38). Consequently, we located line defects in B/Cu and characterized their topographic and electronic properties at the atomic scale. Figure 3A shows two parallel line defects on a B/Cu terrace. A high-resolution

STM topographic image (inset) of the white dashed box reveals the atomic-scale structure of the line defect, where the ~90° turns take place at the ends of longer atomically straight chains compared to the shorter atomically straight chains in the undefective regions. Figure 3B provides another STM image across the double line defects taken with a sharper STM tip, where the atomic chains appear as valley-bridge intermixing patterns due to the participation of different electronic states in the tunneling junction. These observations do not resemble previously reported line defects for borophene (35) and are likely the result of the mismatch with the subsurface copper or the local disorder of the B/Cu layer.

To further assess the electronic properties of the line defects in B/Cu, Fig. 3C shows a constant-current $\partial I/\partial V$ map at 3.3 V (see movie S2 for the full video). A prominent observation is the emergence of the clear rhomboid lattice (marked in red) in the undefective regions. The lattice constants ($a \sim 2.14$ nm and $b \sim 1.57$ nm) match the DFT-calculated Cu_8B_{14} superlattice discussed above. The $\partial I/\partial V$ maps at other energies show different patterns but with similar periodicities (fig. S4). In contrast, the line defects exhibit distinct $\partial I/\partial V$ intensities and features, which is more clearly shown in Fig. 3D, where the $\partial I/\partial V$ spectra of five representative locations (colored circles in Fig. 3C) are plotted together for direct comparison. The distinct characteristics of the line defects include the peaks near 1.96 V (4.15 V) shifting to higher (lower) energy and the disappearance of the peak near 3.3 V that was present in the undefective regions. For better visualization, two series of $\partial I/\partial V$ spectra (from 1.0 to 5.0 V) along the black and gray arrows are shown in Fig. 3 (E and F), respectively. In these spectra, the overall antiphase relationships are evident. Specifically, when the peak near 3.3 V is stronger, the intensities of
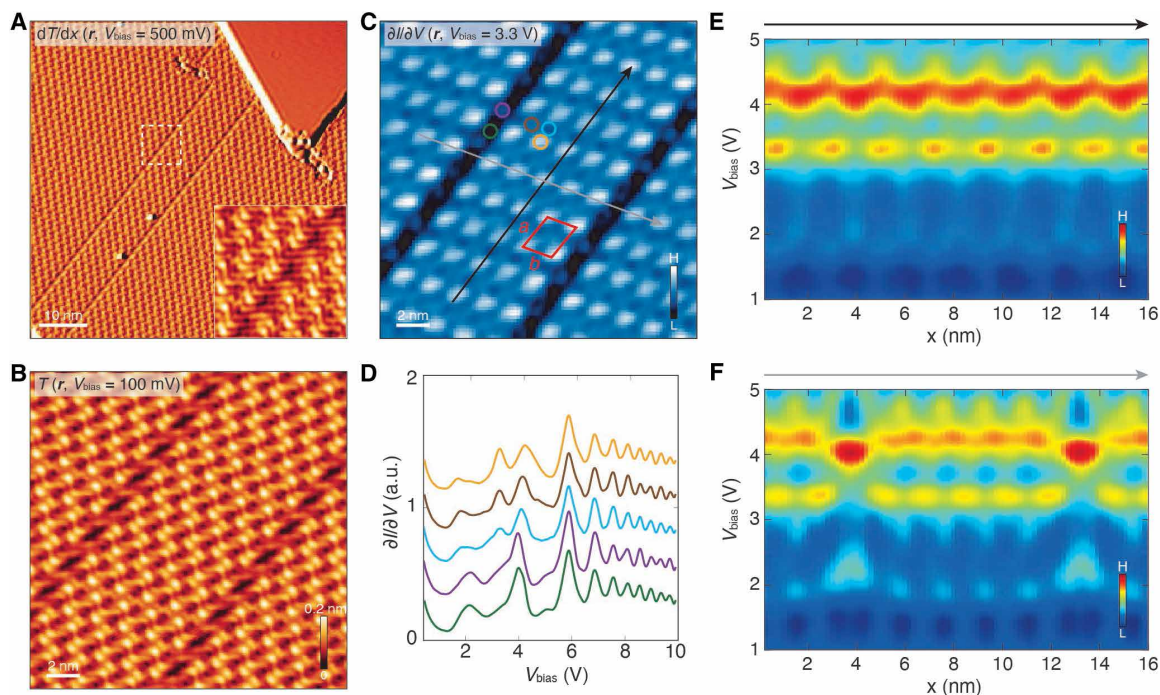

Fig. 3. FER mapping on B/Cu with line defects. (**A**) Derivative STM topography ($V_{bias} = 500$ mV and $I_{setpoint} = 100$ pA) of a B/Cu region with line defects. Inset shows the high-resolution image of the white dashed square. (**B**) STM image of the B/Cu area where the FER mapping is taken. (**C**) The $\partial I/\partial V$ map at $V_{bias} = 3.3$ V extracted from the FER mapping. Apparent rhomboid superlattices can be resolved with lattice constants $a \sim 2.14$ nm and $b \sim 1.57$ nm. (**D**) Five typical FER spectra averaged over the colored circles in (C). The spectra are offset vertically for clarity. (**E** and **F**) FER spectra (1.0 to 5.0 V) extracted along the black and gray arrows in (C), respectively.

the 1.96- and 4.15-V peaks are correspondingly lower. The electronic characteristics of the line defects are especially clear in Fig. 3F, where the stronger intensities of the 1.96- and 4.15-V peaks dwarf the peak near 3.3 V.

Energy maps and correlations of electronic states

In addition to the peak intensities, the peak positions also contain important information about the electronic states. With a precise spatial registration, the energy positions of these peaks on each point can be extracted from the spectroscopic mapping. Figure 4 (A to C) shows the energy maps of those observed peaks below 5.0 V. The line defects appear as long stripes in the 1.96- and 4.15-V peak maps, while the kink positions in the spectra are selected for the extraction of the 3.35-V peak map due to the absence of obvious intensity peaks. Moreover, by applying the fitting with Eq. 1, the LWF of each point can also be extracted to construct the LWF map, as shown in Fig.
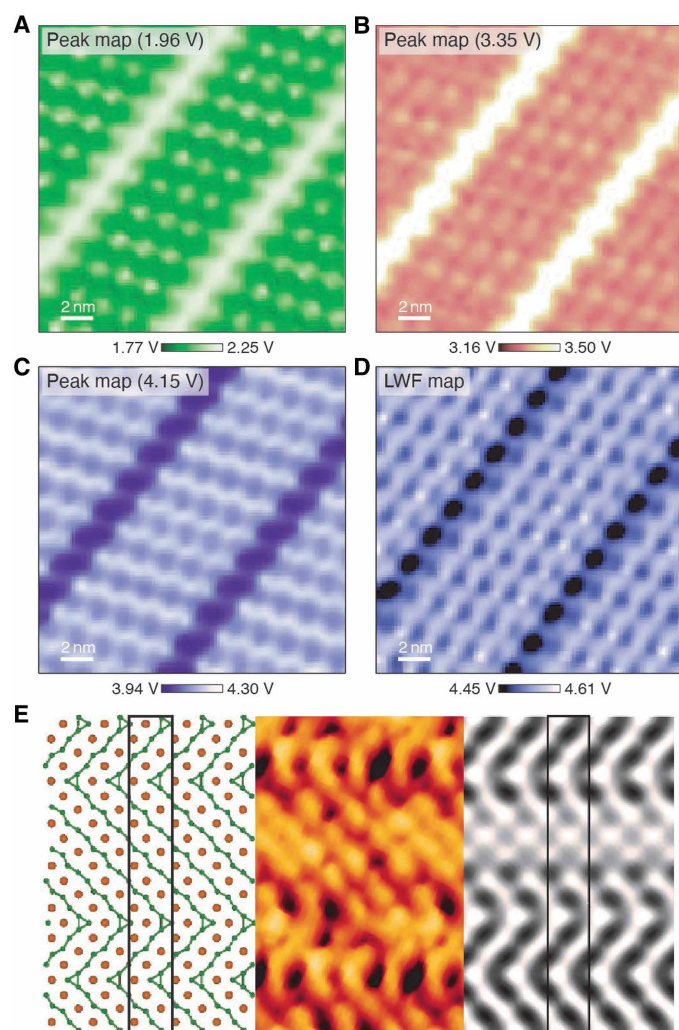
4D. An overall lower LWF is again observed from the line defects, suggesting different charge transfer characteristics for the longer atomically straight chains. Spatial modulations with lattice resolution are present in all of these maps, which further confirm the correlations of the observed peaks (with detailed cross-correlation analysis shown in fig. S5), indicating the likely competition between different electronic states.

As discussed above, the peak near 3.3 V almost disappears at the line defects. The absence of these peaks on defects can be expected when the LDOS of the boron p_z orbitals shifts to higher energies (to merge with the $n = 1$ image potential state) due to a larger amount of charge transfer from copper, which also qualitatively agrees with the LWF results. The effects of atomic orbitals on the correlations of peaks in constant-current spectra have been discussed in previous reports (34–36). Specifically, the antiphase relationships of similar peaks in Cu_3N films were attributed to the half-unit cell shift between different N atoms (36). Because of the similar spectral behavior for Cu_3N and B/Cu, it is likely that the peak near 3.3 V for B/Cu can be attributed to the boron p_z orbital state while the 1.96-V peak is related to an interface state. DFT calculations (fig. S6) of the projected density of states confirm these assignments. The anticorrelations between the low-energy peaks and the higher-energy image potential state can then be expected accordingly, where differences in the charge distributions of different boron orbitals due to local changes in the chemical environment near defects determine the appearance of corresponding spectral features.

The different topographic and spectral characteristics in the line defect regions suggest a distinct assembly of boron and copper atoms in the atomically straight chains. On the basis of the STM images, we constructed a 2D structure including long atomically straight chains and adjacent shorter atomically straight chains with ~90° turns to model the line defect. The left panel of Fig. 4E shows the structural model with a unit cell outlined with a black rectangle. The middle and right panels are the high-resolution experimental STM image and simulated STM image, respectively. The overall agreement between experiment and theory demonstrates that the proposed structure captures the characteristics of the line defects. Minor deviations between experiment and theory can be attributed to the large lattice mismatch with the underlying Cu substrate, which implies an additional longer-range perturbation in the experimental results that is not captured in the smaller unit cell assumed in computationally feasible DFT calculations. Moreover, the $Cu_{11}B_{18}$ stoichiometry in the line defect unit cell suggests a higher concentration of copper compared to pristine Cu_8B_{14}, which also aligns with the charge transfer mechanism that underlies the disappearance of the peaks near 3.3 V. For the 1.96-V peak, the shifts in the LDOS of the boron p_z orbital compete with the electron occupations in the p_x and p_y orbitals, thus also altering the interface states. These observed changes in the electronic states of the line defects reinforce the stability of the Cu_8B_{14} phase and may prove to be useful in applications that rely on electronic structure features far away from the Fermi level such as catalysis (39), valleytronics (40), and neuromorphic memristive devices (41).

Fig. 4. FER energy maps and cross-correlations. (**A** to **C**) Peak maps near 1.96, 3.35, and 4.15 V, respectively. Gaussian fittings are used to extract the peak positions. (**D**) LWF map extracted from a fitting of Stark-shifted image potential states (peaks after $n = 2$). (**E**) From left to right: Structural model, experimental STM topography, and simulated STM image of a B/Cu line defect. Black rectangles indicate the unit cell used in DFT calculations.

DISCUSSION

In conclusion, we have used UHV electron-beam deposition of boron on Cu(111) single crystals to achieve highly ordered 2D B/Cu sheets. Using spatially resolved FER spectroscopic mapping, electronic states

and LWF variations are identified at the atomic scale. The smaller LWF of B/Cu compared to pristine Cu(111) deviates from the typical behavior of a distinct borophene layer on metallic substrates. In addition, the emergence of multiple low-energy FER peaks suggests strong bonding between boron and copper atoms as expected for a 2D copper boride phase. Comparison of these observations with DFT calculations strongly suggests that the 2D copper boride phase is Cu_8B_{14}. Further corroborating evidence is obtained by closely analyzing the physical and electronic structure of line defects for B/Cu. In particular, the line defects are inconsistent with previous observations for distinct borophene layers on metal substrates and are instead attributed to local copper-rich regions in Cu_8B_{14}, as confirmed by DFT-simulated STM images. Overall, this atomically resolved methodology provides strong evidence for the experimental realization of 2D copper boride. The emerging family of 2D metal borides is showing strong potential in a variety of applications, including water splitting (42), batteries (43), and electroreduction (44). The 2D copper boride reported here shows electronic features far from the Fermi level that can potentially be exploited in these applications in addition to atomic-scale LWF modulations that underlie electronic band structure modifications such as bandgap renormalization (45). In this manner, this work can guide synthetic efforts aimed at identifying and characterizing the electronic structure of other 2D metal borides, thus accelerating research for a relatively underexplored family of 2D materials.

MATERIALS AND METHODS

Sample growth

The Cu(111) single crystal was cleaned by repeated Ar^+ sputtering (1 kV, 5.0×10^{-5} mbar) and annealing (~550°C) in a UHV chamber (base pressure $< 2.0 \times 10^{-10}$ mbar). Boron deposition was then performed by electron-beam evaporation of a pure boron rod (ESPI metals, 99.9999% purity) on the heated substrate (~550°C). The accelerating voltage for the evaporator (FOCUS EFM3) was 1800 V, and the filament current was 1.62 A. With a ~5-min boron deposition under a flux of ~9.2 nA, a 60 to 70% coverage of B/Cu domains was obtained on the Cu(111) surface.

STM/STS measurements

All STM/STS measurements were performed with a Scienta Omicron LT STM at ~4 K. The PtIr tip was conditioned by repeated scanning and tip conditioning on the clean Cu(111) surface. The feedback loop was engaged during FER measurements and disengaged for $\partial I/\partial V$ measurements, where both cases were recorded with a SR850 lock-in amplifier with 5-mV bias modulation and 820-Hz frequency. The mapping was conducted only when repeated topographic scans in the interested field of view confirmed that sample drift was negligible. Gaussian fittings were used to extract the peak positions, and LWF was extracted by fitting the image potential states with respect to $n^{2/3}$. Cross-correlation analyses were conducted by the scipy.signal.correlate2d package.

DFT calculations

Structural optimizations and charge distribution calculations were performed by the Vienna Ab initio Simulation Package (46), adopting generalized gradient approximation with the Perdew-Burke-Ernzerhof (47) exchange-correlation functional in the framework of the projector augmented wave method (48). The kinetic energy cutoff was set at 520 eV. The positions of atoms were relaxed until the force of reach atom reached 0.01 eV/Å. The k-mesh was set as 9 by 5 by 1 for $v_{1/6}$ borophene and 3 by 3 by 1 for Cu_8B_{14} copper boride. A vacuum layer of 15 Å was chosen perpendicular to slab surfaces to avoid interactions from the periodic boundary conditions.

Supplementary Materials

The PDF file includes:
Figs. S1 to S6
Legends for movies S1 and S2
References

Other Supplementary Material for this manuscript includes the following:
Movies S1 and S2

REFERENCES AND NOTES

1. A. J. Mannix, X.-F. Zhou, B. Kiraly, J. D. Wood, D. Alducin, B. D. Myers, X. Liu, B. L. Fisher, U. Santiago, J. R. Guest, M. J. Yacaman, A. Ponce, A. R. Oganov, M. C. Hersam, N. P. Guisinger, Synthesis of borophenes: Anisotropic, two-dimensional boron polymorphs. *Science* **350**, 1513–1516 (2015).
2. B. Feng, J. Zhang, Q. Zhong, W. Li, S. Li, H. Li, P. Cheng, S. Meng, L. Chen, K. Wu, Experimental realization of two-dimensional boron sheets. *Nat. Chem.* **8**, 563–568 (2016).
3. W. Li, L. Kong, C. Chen, J. Gou, S. Sheng, W. Zhang, H. Li, L. Chen, P. Cheng, K. Wu, Experimental realization of honeycomb borophene. *Sci. Bull.* **63**, 282–286 (2018).
4. B. Kiraly, X. Liu, L. Wang, Z. Zhang, A. J. Mannix, B. L. Fisher, B. I. Yakobson, M. C. Hersam, N. P. Guisinger, Borophene synthesis on Au(111). *ACS Nano* **13**, 3816–3822 (2019).
5. N. A. Vinogradov, A. Lyalin, T. Taketsugu, A. S. Vinogradov, A. Preobrajenski, Single-phase borophene on Ir(111): Formation, structure, and decoupling from the support. *ACS Nano* **13**, 14511–14518 (2019).
6. K. M. Omambac, M. Petrović, P. Bampoulis, C. Brand, M. A. Kriegel, P. Dreher, D. Janoschka, U. Hagemann, N. Hartmann, P. Valerius, T. Michely, F. J. M. Z. Heringdorf, M. Horn-von Hoegen, Segregation-enhanced epitaxy of borophene on Ir(111) by thermal decomposition of borazine. *ACS Nano* **15**, 7421–7429 (2021).
7. M. G. Cuxart, K. Seufert, V. Chesnyak, W. A. Waqas, A. Robert, M.-L. Bocquet, G. S. Duesberg, H. Sachdev, W. Auwärter, Borophenes made easy. *Sci. Adv.* **7**, eabk1490 (2021).
8. R. Wu, I. K. Drozdov, S. Eltinge, P. Zahl, S. Ismail-Beigi, I. Božović, A. Gozar, Large-area single-crystal sheets of borophene on Cu(111) surfaces. *Nat. Nanotechnol.* **14**, 44–49 (2019).
9. R. Wu, A. Gozar, I. Božović, Large-area borophene sheets on sacrificial Cu(111) films promoted by recrystallization from subsurface boron. *NPJ Quantum Mater.* **4**, 40 (2019).
10. R. Wu, S. Eltinge, I. K. Drozdov, A. Gozar, P. Zahl, J. T. Sadowski, S. Ismail-Beigi, I. Božović, Micrometre-scale single-crystalline borophene on a square-lattice Cu(100) surface. *Nat. Chem.* **14**, 377–383 (2022).
11. C. Chen, H. Lv, P. Zhang, Z. Zhuo, Y. Wang, C. Ma, W. Li, X. Wang, B. Feng, P. Cheng, X. Wu, K. Wu, L. Chen, Synthesis of bilayer borophene. *Nat. Chem.* **14**, 25–31 (2022).
12. P. Sutter, E. Sutter, Large-scale layer-by-layer synthesis of borophene on Ru(0001). *Chem. Mater.* **33**, 8838–8843 (2021).
13. Y. V. Kaneti, D. P. Benu, X. Xu, B. Yuliarto, Y. Yamauchi, D. Golberg, Borophene: Two-dimensional boron monolayer: Synthesis, properties, and potential applications. *Chem. Rev.* **122**, 1000–1051 (2022).
14. Y. Liu, E. S. Penev, B. I. Yakobson, Probing the synthesis of two-dimensional boron by first-principles computations. *Angew. Chem. Int. Ed. Engl.* **52**, 3156–3159 (2013).
15. X.-J. Weng, X.-L. He, J.-Y. Hou, C.-M. Hao, X. Dong, G. Gao, Y. Tian, B. Xu, X.-F. Zhou, First-principles prediction of two-dimensional copper borides. *Phys. Rev. Mater.* **4**, 074010 (2020).
16. C. Yue, X.-J. Weng, G. Gao, A. R. Oganov, X. Dong, X. Shao, X. Wang, J. Sun, B. Xu, H.-T. Wang, X.-F. Zhou, Y. Tian, Formation of copper boride on Cu(111). *Fundam. Res.* **1**, 482–487 (2021).
17. Y. Tsujikawa, M. Horio, X. Zhang, T. Senoo, T. Nakashima, Y. Ando, T. Ozaki, I. Mochizuki, K. Wada, T. Hyodo, T. Iimori, F. Komori, T. Kondo, I. Matsuda, Structural and electronic evidence of boron atomic chains. *Phys. Rev. B* **106**, 205406 (2022).
18. X.-J. Weng, J. Bai, J. Hou, Y. Zhu, L. Wang, P. Li, A. Nie, B. Xu, X.-F. Zhou, Y. Tian, Experimental evidence of surface copper boride. *Nano Res.* **16**, 9602–9607 (2023).
19. C. Buzea, T. Yamashita, Review of the superconducting properties of MgB_2. *Supercond. Sci. Technol.* **14**, R115–R146 (2001).
20. H. J. Choi, D. Roundy, H. Sun, M. L. Cohen, S. G. Louie, The origin of the anomalous superconducting properties of MgB_2. *Nature* **418**, 758–760 (2002).

21. S. Carenco, D. Portehault, C. Boissière, N. Mézailles, C. Sanchez, Nanoscaled metal borides and phosphides: Recent developments and perspectives. *Chem. Rev.* **113**, 7981–8065 (2013).

22. P. R. Jothi, K. Yubuta, B. P. T. Fokwa, A simple, general synthetic route toward nanoscale transition metal borides. *Adv. Mater.* **30**, e1704181 (2018).

23. G. Binnig, K. H. Frank, H. Fuchs, N. Garcia, B. Reihl, H. Rohrer, F. Salvan, A. R. Williams, Tunneling spectroscopy and inverse photoemission: Image and field states. *Phys. Rev. Lett.* **55**, 991–994 (1985).

24. R. S. Becker, J. A. Golovchenko, B. S. Swartzentruber, Electron interferometry at crystal surfaces. *Phys. Rev. Lett.* **55**, 987–990 (1985).

25. D. B. Dougherty, P. Maksymovych, J. Lee, J. T. Yates Jr., Local spectroscopy of image-potential-derived states: From single molecules to monolayers of benzene on Cu(111). *Phys. Rev. Lett.* **97**, 236806 (2006).

26. H.-C. Ploigt, C. Brun, M. Pivetta, F. Patthey, W.-D. Schneider, Local work function changes determined by field emission resonances: NaCl/Ag(100). *Phys. Rev. B* **76**, 195404 (2007).

27. S. Joshi, D. Ecija, R. Koitz, M. Iannuzzi, A. P. Seitsonen, J. Hutter, H. Sachdev, S. Vijayaraghavan, F. Bischoff, K. Seufert, J. V. Barth, W. Auwärter, Boron nitride on Cu(111): An electronically corrugated monolayer. *Nano Lett.* **12**, 5821–5828 (2012).

28. F. Schulz, R. Drost, S. K. Hämäläinen, T. Demonchaux, A. P. Seitsonen, P. Liljeroth, Epitaxial hexagonal boron nitride on Ir(111): A work function template. *Phys. Rev. B* **89**, 235429 (2014).

29. X. Liu, L. Wang, B. I. Yakobson, M. C. Hersam, Nanoscale probing of image-potential states and electron transfer doping in borophene polymorphs. *Nano Lett.* **21**, 1169–1174 (2021).

30. K. Wandelt, The local work function: Concept and implications. *Appl. Surf. Sci.* **111**, 1–10 (1997).

31. O. Y. Kolesnychenko, Y. A. Kolesnichenko, O. I. Shklyarevskii, H. van Kempen, Field-emission resonance measurements with mechanically controlled break junctions. *Physica B: Condens. Matter* **291**, 246–255 (2000).

32. H. B. Michaelson, The work function of the elements and its periodicity. *J. Appl. Phys.* **48**, 4729–4733 (1977).

33. X. Liu, Q. Li, Q. Ruan, M. S. Rahn, B. I. Yakobson, M. C. Hersam, Borophene synthesis beyond the single-atomic-layer limit. *Nat. Mater.* **21**, 35–40 (2022).

34. C. D. Ruggiero, T. Choi, J. A. Gupta, Tunneling spectroscopy of ultrathin insulating films: CuN on Cu(100). *Appl. Phys. Lett.* **91**, 253106 (2007).

35. T. Choi, C. D. Ruggiero, J. A. Gupta, Tunneling spectroscopy of ultrathin insulating Cu$_2$N films, and single Co adatoms. *J. Vac. Sci. Technol. B* **27**, 887–890 (2009).

36. K. Bhattacharjee, X.-D. Ma, Y. Q. Zhang, M. Przybylski, J. Kirschner, Electronic structure of the corrugated Cu$_3$N network on Cu(110): Tunneling spectroscopy investigations. *Surf. Sci.* **606**, 652–658 (2012).

37. A. Eckmann, A. Felten, A. Mishchenko, L. Britnell, R. Krupke, K. S. Novoselov, C. Casiraghi, Probing the nature of defects in graphene by Raman spectroscopy. *Nano Lett.* **12**, 3925–3930 (2012).

38. X. Liu, Z. Zhang, L. Wang, B. I. Yakobson, M. C. Hersam, Intermixing and periodic self-assembly of borophene line defects. *Nat. Mater.* **17**, 783–788 (2018).

39. S. Zhou, W. Pei, Y. Zhao, X. Yang, N. Liu, J. Zhao, Low-dimensional non-metal catalysts: Principles for regulating p-orbital-dominated reactivity. *NPJ Comput. Mater.* **7**, 186 (2021).

40. J.-H. Chen, G. Autès, N. Alem, F. Gargiulo, A. Gautam, M. Linck, C. Kisielowski, O. V. Yazyev, S. G. Louie, A. Zettl, Controlled growth of a line defect in graphene and implications for gate-tunable valley filtering. *Phys. Rev. B* **89**, 121407 (2014).

41. V. K. Sangwan, H.-S. Lee, H. Bergeron, I. Balla, M. E. Beck, K.-S. Chen, M. C. Hersam, Multi-terminal memtransistors from polycrystalline monolayer molybdenum disulfide. *Nature* **554**, 500–504 (2018).

42. S. Gupta, M. K. Patel, A. Miotello, N. Patel, Metal boride-based catalysts for electrochemical water-splitting: A review. *Adv. Funct. Mater.* **30**, 1906481 (2020).

43. J. Jia, B. Li, S. Duan, Z. Cui, H. Gao, Monolayer MBenes: Prediction of anode materials for high-performance lithium/sodium ion batteries. *Nanoscale* **11**, 20307–20314 (2019).

44. X. Guo, S. Lin, J. Gu, S. Zhang, Z. Chen, S. Huang, Establishing a theoretical landscape for identifying basal plane active 2D metal borides (MBenes) toward nitrogen electroreduction. *Adv. Funct. Mater.* **31**, 2008056 (2021).

45. Q. Zhang, Y. Chen, C. Zhang, C.-R. Pan, M.-Y. Chou, C. Zeng, C.-K. Shih, Bandgap renormalization and work function tuning in MoSe$_2$/hBN/Ru(0001) heterostructures. *Nat. Commun.* **7**, 13843 (2016).

46. G. Kresse, J. Furthmüller, Efficient iterative schemes for ab initio total-energy calculations using a plane-wave basis set. *Phys. Rev. B Condens. Matter* **54**, 11169–11186 (1996).

47. J. P. Perdew, K. Burke, M. Ernzerhof, Generalized gradient approximation made simple. *Phys. Rev. Lett.* **77**, 3865–3868 (1996).

48. P. E. Blöchl, Projector augmented-wave method. *Phys. Rev. B* **50**, 17953–17979 (1994).

49. X. Liu, L. Wang, S. Li, M. S. Rahn, B. I. Yakobson, M. C. Hersam, Geometric imaging of borophene polymorphs with functionalized probes. *Nat. Commun.* **10**, 1642 (2019).